



HAL
open science

Smoke on the wind: dust nucleation in archetype colliding wind pinwheel WR 104

A. Soulain, A. Lamberts, F. Millour, P. Tuthill, R. M. Lau

► **To cite this version:**

A. Soulain, A. Lamberts, F. Millour, P. Tuthill, R. M. Lau. Smoke on the wind: dust nucleation in archetype colliding wind pinwheel WR 104. *Monthly Notices of the Royal Astronomical Society*, 2022, 10.1093/mnras/stac2999 . insu-03860273

HAL Id: insu-03860273

<https://insu.hal.science/insu-03860273>

Submitted on 7 Apr 2023

HAL is a multi-disciplinary open access archive for the deposit and dissemination of scientific research documents, whether they are published or not. The documents may come from teaching and research institutions in France or abroad, or from public or private research centers.

L'archive ouverte pluridisciplinaire **HAL**, est destinée au dépôt et à la diffusion de documents scientifiques de niveau recherche, publiés ou non, émanant des établissements d'enseignement et de recherche français ou étrangers, des laboratoires publics ou privés.

Smoke on the wind: dust nucleation in the archetype colliding-wind pinwheel WR 104

A. Soulain ^{1,2★}, A. Lamberts,^{3,4} F. Millour,³ P. Tuthill² and R. M. Lau⁵

¹Université Grenoble Alpes, CNRS, IPAG, 38100 Grenoble, France

²School of Physics, University of Sydney, NSW 2006, Australia

³Université Côte d'Azur, Observatoire de la Côte d'Azur, CNRS, Laboratoire Lagrange, Bd de l'Observatoire, CS 34229, F-06304 Nice cedex 4, France

⁴Université Côte d'Azur, Observatoire de la Côte d'Azur, CNRS, Laboratoire Artémis, Bd de l'Observatoire, CS 34229, F-06304 Nice cedex 4, France

⁵NSF's NOIR Lab, 950 N. Cherry Avenue, Tucson, AZ 85721, USA

Accepted 2022 October 14. Received 2022 October 13; in original form 2022 August 9

ABSTRACT

A handful of binary Wolf–Rayet stars are known to harbour spectacular spiral structures spanning a few hundred astronomical units. These systems host some of the highest dust production rates in the Universe and are therefore interesting candidates for addressing the origin of the enigmatic dust excess observed across galactic evolution. The substantial interaction between the winds of a Wolf–Rayet star and its companion constitutes a unique laboratory in which to study the mechanisms of dust nucleation in a hostile environment. Using the grid-based `RAMSES` code, we investigate this problem by performing a 3D hydrodynamic simulation of the inner region of the prototypical spiral nebula around WR 104. We then process the `RAMSES` results using the radiative transfer code `RADMC3D` to generate a candidate observable scene. This allows us to estimate the geometrical parameters of the shocked region. We link these quantities to the specific chemical pathway for dust nucleation, where the hydrogen-rich companion's wind catalyses dust formation. The scaling laws we derive constitute a unique tool that can be directly compared with observations. Depending on the dust nucleation locus, the velocity field reveals a differential wind speed, implying that the initial dust speed could be more balanced between the speeds of the two stellar winds ($\sim 1600 \text{ km s}^{-1}$). With `RADMC3D`, we provide constraints on the dust nucleation radius for different combinations of the dust-to-gas ratio, hydrogen fraction, and dust grain properties. Finally, our models reveal that dust may escape beyond the boundaries of the spiral owing to hydrodynamical instabilities in the wind collision zone.

Key words: hydrodynamics – radiative transfer – circumstellar matter – stars: winds, outflows – stars: Wolf–Rayet.

1 INTRODUCTION

Classical Wolf–Rayet (WR) stars are the immediate precursor stage to the supernova explosion of massive stars. Massive stars are thought to be responsible for much of the chemical evolution of galaxies, playing their part in chemical enrichment and injecting kinetic energy that acts to moderate stellar formation. WR stars play a crucial role in governing the proportion of observed carbon (^{14}C) or aluminium (^{26}Al) elements in the local interstellar medium, which are key ingredients of solar-like planetary systems (Tatischeff, Duprat & de Séréville 2010). These direct descendants of massive O-type stars are characterized by a dense ($> 10^{-5} \text{ M}_{\odot} \text{ yr}^{-1}$), fast ($> 1000 \text{ km s}^{-1}$) and optically thick radiative wind that can entirely shroud the photosphere. Notwithstanding the violent conditions around WR stars that at first sight appear sterile for dust, a significant infrared excess emerges from spectroscopic determinations (Allen, Swings & Harvey 1972; Williams, van der Hucht & The 1987). Depleted of their hydrogen-rich shells, the early nitrogen-rich WR stars (WN subgroup) evolve into the late carbon-rich stage (WC subgroup) and, in some cases, initiate an era of efficient dust production. Despite their relatively short lifespan ($< 1 \text{ Myr}$; Groh et al. 2014) and their

being one of the rarest types of star in the Milky Way (~ 670 ; Rosslowe & Crowther 2015), WCs are thought to be a significant contributor to the galactic dust reservoir. In fact, decades of infrared surveys highlight an excess of galactic dust both locally (Matsuura et al. 2009; Boyer et al. 2012; Srinivasan et al. 2016) and at high redshift (Rowlands et al. 2014). Recently, Lau et al. (2020a) revisited the impact of dust production from the Galactic WC population using a sample of 19 carbon-rich WR stars. Their spectral energy distribution (SED) comparison revealed a high dust production rate (DPR, $\dot{M}_d \sim 10^{-10} - 10^{-6} \text{ M}_{\odot} \text{ yr}^{-1}$) with a wide variety of carbon condensation fractions (0.002–40 per cent). Such DPRs can be compared with Galactic evolution models and thus could imply that WC stars dominate galactic dust budgets at stages prior to the arrival of numerous low-mass evolved giant stars the Asymptotic Giant Branch stars (AGBs). The case for extragalactic WC stars dominating dust production is even more compelling, particularly in low-metallicity environments (Lau et al. 2021).

The WR system WR 104 (MR80) represents the prototype of such a dust producer. Initially, the presumption of dust formation was evoked to explain the large infrared excess observed by Allen et al. (1972). The first attribution as a pinwheel nebula came from the first reconstructed image of the system by Tuthill, Monnier & Danchi (1999) using the non-redundant masking (NRM) technique (Baldwin et al. 1986; Tuthill et al. 2000). WR 104 benefitted from

* E-mail: anthony.soulain@univ-grenoble-alpes.fr

intensive follow-up observations to understand its properties and constrain the orbital period (241.5 d) of its central binary (Tuthill et al. 2008). In the early 2000s, space-based observations with the *Hubble Space Telescope* (*HST*) revealed a second companion (‘companion B’) at a larger separation (Wallace, Moffat & Shara 2002). A more recent study led by our team confirmed the gravitational link with companion B, but this companion appears to have no impact on the spiral shape itself (Soulain et al. 2018). The distance to the system (2.5 ± 0.1 kpc) is estimated following the method adopted by Tuthill et al. (2008). As the dust and gas are expected to be coextensive, the dust expansion speed is attributed to the terminal wind speed of the dominant WR star (1220 km s^{-1} measured by spectroscopy; Howarth & Schmutz 1992). This assumption could be more complex than expected, as recently highlighted by the important discrepancy detected between the spectroscopic and the dust velocities in the Apep system (Han et al. 2020). An extensive study concerning the velocity field is therefore required to unravel the relationship between the gas and the dust grains involved in such binary systems.

Despite the hostile thermal and radiative environment, one mechanism for dust formation in WC stars is mediated by colliding-wind binary interactions, as proposed by Usov (1991). The apparent necessity to include a massive companion is consistently reinforced by both observations (Tuthill et al. 2008; Millour et al. 2009; Han et al. 2020) and simulations (Lamberts et al. 2012; Hendrix et al. 2016). Notably, massive stars are commonly (potentially always) involved in multiple systems (Sana et al. 2013). A recent spectroscopic survey by Dsilva et al. 2020 showed that 70 per cent of Galactic WR stars are in multiple systems. This suggests that a large fraction of massive stars could potentially present a dust production episode during their lifetime.

The wind collision zone (WCZ) generated by massive binary stars can protect the dust nucleation from the intense stellar UV radiation. Numerical simulations show that shocked winds are separated from each other by a contact discontinuity, which may be subject to various instabilities (Stevens, Blondin & Pollock 1992). The innermost hydrodynamic structure is imposed by the winds’ momentum flux ratio and radiative cooling. For WR 104, we anticipate that the shock surface will be heavily skewed towards the O-star companion, which boasts a much less dense (and hence lower-momentum) wind. Further out, orbital motion wraps the shocked structure into a spiral shape (Lamberts et al. 2012).

While analytic estimates provide the location of the shocked region between the stars and the asymptotic opening angle of the WCZ (Myasnikov & Zhekov 1993), hydrodynamic simulations are essential to capture the complete 3D geometry of the interaction region. Only numerical simulations provide a comprehensive model of the density, velocity, and temperature conditions in the WCZ (Pittard 2009). Such efforts have been extensively used to constrain X-ray observations (Pittard et al. 2005) or the gaseous structure of the dustless system γ Vel by interferometry (Lamberts et al. 2017). Hendrix et al. (2016) investigated the effects of radiative cooling at larger scales, revealing a dramatic impact on the opening angle compared with previous studies. By including dust directly in their hydrodynamical modelling, these authors were able to retrieve the realistic density structure of the massive binary WR98a, a system similar to WR104, harbouring a pinwheel nebula (Monnier, Tuthill & Danchi 1999). Such spiral patterns have also been observed around massive red giant binary systems, as recently modelled by Castellanos-Ramírez et al. (2021). The binary interaction is also evoked to explain the 3D gaseous structures observed by Atacama Large Millimeter/submillimeter Array (ALMA) around massive stars (Maercker et al. 2012).

Following these simulation efforts, we present our new `RAMSES` simulation of the very inner region of the system WR 104. We focus our attention on the first 50 au, where the dust is expected to form, as constrained by observations (Soulain et al. 2018). Our aims are (1) to understand the role of the companion in terms of the hydrogen fraction, (2) to link the spiral morphology and the physics of the dust nucleation, (3) to estimate the velocity map at the expected dust formation locus, and (4) to constrain the nucleation radius using radiative transfer modelling. The exquisite spatial resolution afforded by restricting the region of interest allows us to delve into the underlying physics of the dust nucleation processes.

Our paper is organized as follows. In Section 2, we discuss the numerical method and the initial and boundary conditions of the simulations. We also present the adopted methodology to compute the dust density grid. Section 3 describes our radiative transfer approach applied to post-process the `RAMSES` simulation using the `RADMC3D` code. In Section 4, we present the results focusing on the spiral morphology, velocity determinations, and nucleation radius. In Section 5, we interpret and discuss the astrophysical consequences of our results, and finally, in Section 6, we conclude and place this effort into a wider astrophysical context.

2 HYDRODYNAMICAL SIMULATION

2.1 Numerical setup and initialization of the stellar winds

We use the `RAMSES` code, which is based on a second-order Godunov method (Teyssier 2002), to numerically solve the system of hydrodynamics equations:

$$\begin{aligned} \frac{\partial \rho}{\partial t} + \nabla \cdot (\rho \mathbf{v}) &= 0 \\ \frac{\partial (\rho \mathbf{v})}{\partial t} + \nabla \cdot (\rho \mathbf{v} \mathbf{v}) + \nabla P &= 0 \\ \frac{\partial E}{\partial t} + \nabla \cdot [\mathbf{v}(E + P)] &= n^2 \Lambda(T), \end{aligned} \quad (1)$$

where ρ is the density, \mathbf{v} is the velocity, P is the pressure of the gas, and n is the number density. Λ is the radiative cooling rate of the gas, based on Sutherland & Dopita (1993). The cooling curve assumes an optically thin gas in ionization equilibrium. We assume a solar abundance for the O-star wind and a WR abundance for the WR wind (Stevens et al. 1992), which leads to increased cooling. We set the adiabatic index $\gamma = 5/3$, and the total energy density E is given by

$$E = \frac{1}{2} \rho v^2 + \frac{P}{(\gamma - 1)}. \quad (2)$$

To distinguish between the two winds and quantify their mixing rate, we include a passive scalar, advected by each wind. To limit the numerical quenching of hydrodynamic instabilities, we use the MinMod slope limiter combined with the HLLC Riemann solver.

The simulation is based on a Cartesian grid with outflow boundary conditions. To study the dust condensation region, the simulation domain is 24 times the semimajor axis of the binary ($a = 2.34 \text{ au}^1$). The orbital plane is set at $z = 0$, and we initialize the binary in the upper left corner of the domain. This allows us to model the interaction region with optimized computational cost. The simulation is stopped after 30 per cent of one orbital period. The default

¹We applied Kepler’s second law with $M_{\text{WR}} = 10M_{\odot}$ (Sander, Hamann & Todt 2012), $M_{\text{OB}} = 20M_{\odot}$ (Fierro et al. 2015) and $P = 241.5 \text{ d}$.

Table 1. Wind parameters in the hydrodynamic simulation.

Parameter		Reference
$v_{\infty/\text{WR}}$	1220 km s ⁻¹	Howarth & Schmutz (1992)
\dot{M}_{WR}	$0.8 \times 10^{-5} M_{\odot} \text{ yr}^{-1}$	Monnier et al. (2002)
$v_{\infty/\text{OB}}$	2000 km s ⁻¹	Harries et al. (2004)
\dot{M}_{OB}	$0.5 \times 10^{-7} M_{\odot} \text{ yr}^{-1}$	Fierro et al. (2015)

resolution of the simulation is $N_x = 256$, and we allow up to five levels of adaptive mesh refinement (AMR) to locally increase the resolution for a limited computational cost. AMR is limited to 10 per cent of the simulation domain above and below the mid-plane. The three highest levels of refinement (equivalent resolution of $N_x = 2048$ and above) are restricted to smaller and smaller regions around the stars. The high resolution is necessary to ensure the spherical symmetry of the winds and guarantee that the shock region can develop naturally. Because of the strongly unequal winds, the shocks develop close to the O star, and enough computational cells are necessary for this narrow region. Our physical resolution is about 0.007 au, which should yield limited numerical heat conduction at the interface between the winds (Parkin & Pittard 2010).

The winds are generated following the same method as in Lamberts, Fromang & Dubus (2011) and Lamberts et al. (2017). A density, pressure and velocity profile is set at each time-step within a small region representing the star. Table 1 shows the wind parameters for our simulation. The winds are highly supersonic, and we set their Mach number to 30. The corresponding temperature is higher than expected in stellar winds but allows for numerical stability. In this case, the shocked region is mostly unaffected by the value of the pre-shock temperature. The orbital motion of the stars is determined using a leapfrog method. As the orbital velocity is negligible with respect to the speed of the winds, each wind can be considered isotropic in the frame co-rotating with the corresponding star.

2.2 Spatial sampling of RAMSES quantities

The strong density and pressure gradients occurring in the system impose a high refinement along the wind–wind collision interface, as shown in detail by Lamberts et al. (2011, 2012). The shocked zone is also a region of important cooling, which can be correctly modelled only with a high spatial resolution (van Marle & Keppens 2011). While this is necessary for an accurate representation of the hydrodynamics of the system, this high number of cells is unnecessarily challenging for the radiative effects we focus on in post-processing.

To retrieve an accurate spatial sampling of the RAMSES outputs and interface them with the radiative transfer code (Section 3.2), we interpolate the final output of the simulation over a 3D linear spatial grid. We used the PYTHON–RAMSES interface PYMSES² to sample the different hydrodynamical quantities, namely the gas density (g cm⁻³), the pressure (g cm⁻¹ s⁻²), and the velocity field (cm s⁻¹). The 3D simulation implies a significant increase of elements with the resolution (factor $2^3 = 8$) and requires that the sampling parameter N is chosen carefully. The primary (non-refined) grid of the RAMSES simulation is sampled over 256^3 elements. We choose this value to sample our final grid. The AMR refinement occurs mainly in the regions of highest density (i.e. between the two stars and in the immediate surroundings of the WR star); it becomes negligible far

from the central core, where the dust is expected to form. To ensure that the adopted resolution ($N_r = 256$) is sufficient for our purpose, we realize a series of tests using half (128), twice (512) and four times (1024) the RAMSES resolution and compute the relevant quantifiable radiative outputs (integrated fluxes, temperatures), which will be described later (Section 4.3). It appears that both the temperatures and the fluxes reach a plateau around the adopted resolution (i.e. the equilibrium state) and do not exhibit significant variation after this limit (< 1 per cent). We note that our results on the geometrical aspect of the wind collision region (Section 4.1) are independent of the chosen sampling.

2.3 Chemical composition and dust formation

To retrieve the 3D geometrical structure of the dust formed within the WCZ, it is necessary to convert the gas grid obtained with RAMSES into a usable dusty grid. The exact processes of carbonaceous grain nucleation and subsequent growth are complex and have been studied in various environments, such as supernovae ejecta (Lazzati & Heger 2016; Heays et al. 2017), massive stars (Cherchneff et al. 2000), and AGB stars (Gobrecht et al. 2017; Bladh et al. 2019). Dust results from a chemical cascade of elemental reactions (radiative combination, molecule–ion reactions, photo-dissociation), initially forming carbon chains of tens of atoms. Those chains then condense other molecular species up to micrometre size, thus constituting the so-called dust. For the particular case of the WR star environment, Cherchneff et al. (2000) showed that these carbon chains (typically above six atoms) could only be generated in a dense environment ($\rho > 10^{-14}$ g cm⁻³). Such high densities are present in our simulation but in regions that are too close to the stars to allow the dust to survive (because of above-sublimation temperatures). Another way to form carbon dust is to react acetylene molecules (C₂H₂) to form polyaromatic hydrocarbons (PAHs), which are themselves thought to be precursors of amorphous carbon grains (Dhanoa & Rawlings 2014). This second route requires a relatively strong abundance of hydrogen to be effective. Assuming this latter mechanism, we estimate that the most likely zone for efficient dust formation is the mixing zone of the two stellar winds, where the wind of the H-rich main-sequence companion will enrich the wind of the C-rich WR star.

To track the relative chemical composition of the fluid inside the simulation, we define two fluid tracers, χ_C and χ_H . They denote the relative proportions of the C-rich WR wind and the H-rich B-star wind in the gas. These two tracers are initialized (to 0 or 1) in each star at each time-step, along with the other hydrodynamical quantities. They then evolve freely on the grid. We focus our study on the chemical content of the gas allowing, under certain hypotheses, significant dust formation. We use the local product of the tracers to retrieve the effective mixing of the material in the fluid. The mixing factor is computed as $\zeta = \chi_C \chi_H$, where $\zeta = 0.25$ represents a gas composed equally of H-rich and C-rich wind. This so-called mixing region will trace the WCZ and will make up the ideal locus to form dust efficiently.

To study the impact of the hydrogen-fraction hypothesis, we compute several values of $\chi_{H/C}$ from 1 to 40 per cent, logarithmically spaced. We chose a logarithmic sampling to focus on the turbulent zone we identified in the low-mixing regime (< 5 per cent, Section 4.1). In the following, we adopt the formalism $\chi_{H/C}$ to represent the fraction of hydrogen or carbon regarding the contact discontinuity (CD): a $\chi_{H/C}$ of 1 per cent indicates that the fraction of hydrogen is at least 1 per cent (99 per cent for the carbon) in the C-rich wind (outside the CD) and 99 per cent (1 per cent for C) in the H-rich wind (inside the CD). Formally, the corresponding mixing factor ζ will be

²<http://irfu.cea.fr/Projets/PYMSES/intro.html>

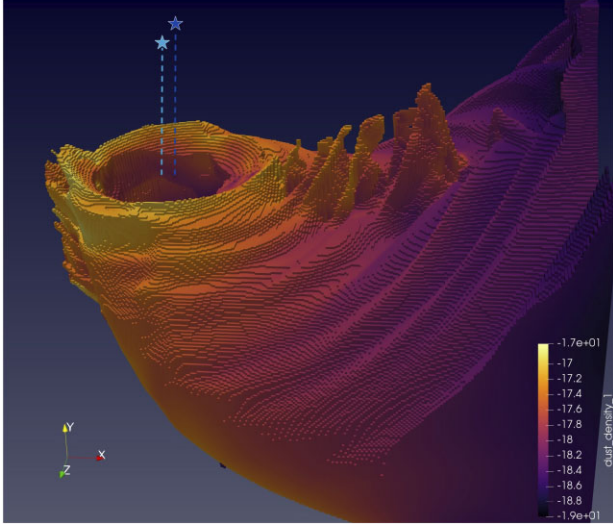


Figure 1. 3D view of an arbitrary dust density grid ($\chi_{\text{H/C}} = 5$ per cent, $\xi = 0.5$ per cent, and $r_{\text{nuc}} = 15$ au). We note the gas/dust plume in the XY -plane resulting from the Kelvin–Helmholtz instability. The positions of both stars are represented (light blue, OB star; blue, WR star).

set between 0.0099 (1 per cent–99 per cent) and 0.24 (40 per cent–60 per cent).

We use the linearly sampled grid of the gas density described above (Section 2.2) and the mixing factor ζ to place the dust in the grid artificially. We consider that dust is present in all grid elements where ζ reaches a certain value. We then compute the dust density grid by applying a gas-to-dust ratio ξ_{dust} .

Finally, we use an additional parameter called the nucleation radius r_{nuc} to mimic the dust formation locus. Therefore, we set the dust density to zero in a sphere of radius r_{nuc} around the WR star. This additional parameter allows us to investigate the sublimation temperature of the dust (Section 3.2). We note that this work does not consider the gas temperature retrieved by the `RAMSES` simulation.

Fig. 1 shows an example of a 3D representation of the dust grid ($\chi_{\text{H/C}} = 5$ per cent, $\xi = 0.5$ per cent, and $r_{\text{nuc}} = 15$ au), where the density is colour coded. We also show the positions of both stars (from the `RAMSES` grid) for reference.

3 RADIATIVE TRANSFER MODELLING

3.1 Post-processing of the hydrodynamics simulation

We use a radiative transfer approach to post-process the dust grid of our `RAMSES` simulation. The model covers the inner region of the system (56 au) with a very high spatial resolution (0.007 au), allowing us to pinpoint the dust nucleation radius precisely. As previously noted, the dust grid is computed using only the gas density grid, a gas-to-dust ratio, a mixing factor, and a nucleation radius. Thereby, the aspects of dust sublimation and survival are not considered *a priori* and need to be inferred from the simulation in an iterative procedure.

3.1.1 `RADMC3D`

We used the radiative transfer code `RADMC3D` (Dullemond et al. 2012) to determine the dust temperature and the associated dust sublimation radius (Section 4.3).

Table 2. Adopted and refined stellar parameters.

	WR star (WC9)	B star (B2V)
T_*	45 000 K	30 000 K
R_*	6 R_{\odot}	13.5 R_{\odot}
L_*	140 000 L_{\odot}	130 000 L_{\odot}

The robustness and accuracy of the code were validated in the benchmark analysis from Pinte et al. (2009). `RADMC3D` calculates the temperature distribution of dusty environments based on a Monte Carlo method proposed by Bjorkman & Wood (2001). In practice, a large number (typically hundreds of millions) of packets of photons are launched individually, carrying an amount of energy proportional to the total luminosity of the radiation source. Each packet travels through the model dust grid and is absorbed and re-emitted or scattered until it reaches the edge of the grid or disappears (where the optical depth is above 30). After the launch of many photon packets, the equilibrium temperature is then usually reached at each point on the grid. The scattering source function is then calculated for each wavelength using an additional Monte Carlo iteration. We adopt isotropic scattering, justified by the use of small dust grains (0.1 μm , Section 3.1.3).

3.1.2 Stellar parameters

To represent the SEDs of our system, we used the `PoWR`³ atmosphere model for the WR star (Sander et al. 2012) and the Kurucz model for the massive companion⁴ (Castelli & Kurucz 2004). These advanced atmosphere models enable one to consider the complex phenomena occurring in the photosphere, including emission and absorption features.

Besides the general aspect of the SED, it is necessary to normalize both spectra to compute a realistic total luminosity. Previous estimates appeared to be too coarse owing to the important reddening occurring in this galactic region ($A_v = 6.67$; Rate & Crowther 2020). Crowther (1997) reported a total luminosity of 120 000 L_{\odot} with a luminosity ratio (WR:OB) of 0.5, giving $L_{\text{WR}} = 40 000 L_{\odot}$, well under the modelled estimations of a single WR star (Sander et al. 2019). Therefore, we refine this estimate using the high-precision magnitudes provided by the *Gaia* Data Release 2 (Gaia Collaboration et al. 2018). We use the visual extinction to unreddened the three *Gaia* magnitudes (BP, G, and RP). We then normalize the atmosphere models using the luminosity of both components with the Stefan–Boltzmann relation ($L_* = 4\pi R_*^2 \sigma T_*^4$). We set the effective temperatures to 45 000 K and 30 000 K for the WR and the B star, respectively, and use the stellar radii as free parameters. Using the spectroscopic information, we set the intensity ratio in the v band (0.5 μm) to 0.5 (Crowther 1997), where the B star is twice as bright as the WR star. We finally adjust the stellar radii to fit the unreddened *Gaia* magnitudes using a distance of 2.58 kpc (Soulain et al. 2018). We obtain a total refined luminosity of 270 000 L_{\odot} (Table 2).

³We used the 2018 version of the WC 06-11 model, the Potsdam Wolf-Rayet Models, http://www.astro.physik.uni-potsdam.de/~wrh/PoWR/powr_grid2.php.

⁴We chose the spectral type B0V (close to B2V) with $\log(g) = 4$.

3.1.3 Dust properties

The dust grain-size distribution in WC stars is still debated, ranging from a unique small size of $a = 0.01 \mu\text{m}$ (Zubko 1998; Williams et al. 2009) to a large $a > 0.5 \mu\text{m}$ (Chiar & Tielens 2001; Marchenko et al. 2002). In order to proceed in the face of this controversy, we consider three different grain-size hypotheses: *small*, *large*, and *unique*. Similarly to in Lau et al. (2020a), the *small* (*large*) grain-size distribution includes grains in the range $a = 0.01\text{--}0.1 \mu\text{m}$ ($0.1\text{--}1 \mu\text{m}$) with a number density distribution proportional to $n(a) \propto a^{-3}$. The *unique* grain size hypothesis (i.e. $a = 0.01 \mu\text{m}$) stands for the rapid growth of the dust nuclei limited by the high wind-speed velocity (Zubko 1998).

We assume that the dust grains are composed of purely amorphous carbon grains, as suggested by both observations and simulations (Williams et al. 1987; Zubko 1998; Harries et al. 2004). The optical constants of the amorphous carbon, represented by the refractive indices (real and imaginary parts), are taken from the database at Jena University (<http://www.astro.uni-jena.de/Laboratory/OCDB/>). The mass absorption and scattering coefficients, κ_{abs} and κ_{sca} , are then computed from these optical constants for the three distribution hypotheses. We consider irregularly shaped grains, approximated by a distribution of hollow spheres (DHS; Min, Hovenier & de Koter 2005).

3.1.4 Static mesh refinement

In addition to the linear grid used to represent the dust distribution, we perform an additional refinement step before applying the radiative transfer computation. For the Monte Carlo calculation by RADMC3D, it is essential that the first encountered grid element is optically thin ($\tau < 1$). Otherwise, the packet of photons could be caught in this first cell and not contribute to thermalizing the overall grid. This effect is demonstrated using RADMC3D on massive thick discs, which produces intensity artefacts on the images (Dullemond et al. 2012).

We increase the spatial resolution locally by dividing the selected cell into eight subcells (in 3D). These subcells can then be divided until reaching the desired optical depth. We applied this refinement to optically thick cells, increasing the level of static mesh refinement (SMR) to obtain a global optically thin grid. To be conservative and independent of the spectral domain, we performed the refinement using a unique set of absorption and scattering coefficients (κ_{abs} , κ_{sca}). We chose the maximal sum of those coefficients (κ_{max}) compared with the wavelength, and set the limit of the optical depth with

$$\tau = \rho \kappa_{\text{max}} V_{\text{cells}} \geq 1, \quad (3)$$

where ρ is the density of a grid element and V_{cells} is its volume.

3.2 Modelling approach

In order to determine the nucleation radius imposed by the considered grain-size distributions (*small*, *large*, and *unique*), we perform a series of radiative transfer computations covering a range of nucleation radii from 15 to 35 au, with a 2.5-au step. This range of spatial scales is motivated by previous observational determinations of the nucleation radius by Tuthill et al. (2008) and Soulain et al. (2018). Both of these papers report a very similar dust sublimation radius of around 12 mas (≈ 31 au at the distance of the WR104 system). These measurements were inferred using the observed offset between the peak emission of the dusty spiral structure and the initial point of the fitted Archimedean spiral. Our models cover a broad range of solutions to be sure to include the expected position of this important

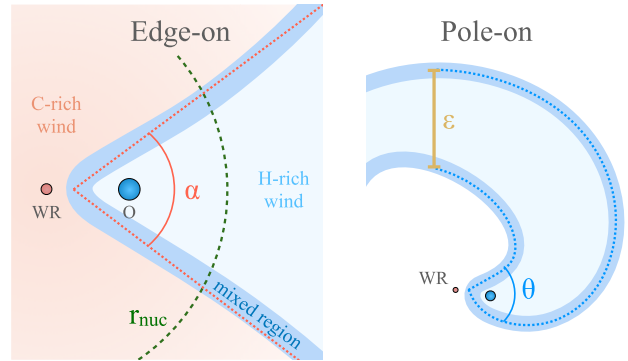


Figure 2. Schematic view of the system presenting the different angles and parameters mentioned in this work. Left: wind–wind collision zone seen from the orbital equator (similar to Fig. 3). Right: extrapolated spiral seen pole-on.

physical parameter. To examine the impacts of the dust production efficiency, we implement a range of gas-to-dust ratios ($\xi_{\text{dust}} = 0.1, 1, 3, 5, 7, 10$ per cent) and mixing factors ($\chi_{\text{H}} = 1, 5, 10, 20$ per cent) for each nucleation radius, which results in 648 models in total.

The choice of the dust grain composition is essential for inferring the dust nucleation radius imposed by its sublimation temperature. For carbonaceous dust, the sublimation temperature is supposed to be around 2000 K (Kobayashi et al. 2011). In the following, we use the term ‘hot dust’ to refer to all dust cells presenting an equilibrium temperature above the considered sublimation temperature. If the relative proportion of hot dust becomes significant, we consider the associated radius as too close to be realistic and use the closest non-hot radius as the measured nucleation radius.

4 RESULTS AND ANALYSIS

4.1 Parameters arising from mixing

In this section, we present the results from the hydrodynamical modelling. Fig. 2 shows the global geometry of the interaction region and the parameters we will be using. The goal is to arrive at a physical intuition for the geometrical parameters obtained by fitting the observations.

4.1.1 Dust opening angle versus shocked wind–wind interface

The first parameter we investigate is the full-opening angle α . It represents the conical flare of the shocked interface between the two spherical winds. Eichler & Usov (1993) state that the analytical solution is proportional to the momentum flux balance of the two stellar winds. In the case of WR 104, the quantities involved give $\alpha \approx 40^\circ$, yielding one quantitative comparison to confront our numerical estimation with observation.

We derive the opening angle for each mixing value from 0.0099 to 0.24, representing the hydrogen fraction of the gas (Section 2.3). We use a Laplacian filter applied on the edge-on projected grid to fit both sides of the cone. In order to detect the edges automatically, we add distance and density conditions to avoid a strong deformation of the central region (Fig. 3). We use a Levenberg–Marquardt minimization to determine both the values and the statistical uncertainties of α , recovering an average precision of $\sigma_\alpha = 0.6$. The adjusted parameters are plotted in Fig. 4, illustrating the two most extreme values of mixing ($\chi_{\text{H/C}} = 1$ per cent and 40 per cent) under consideration.

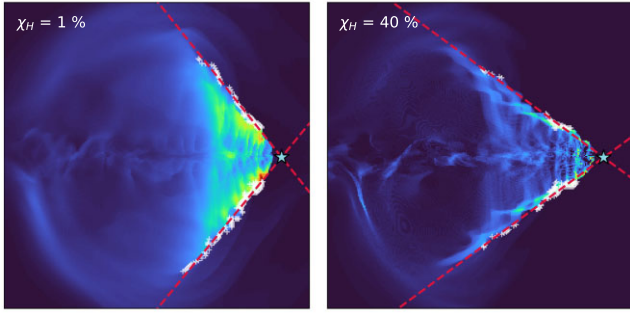


Figure 3. Example fits to the opening angle on the projected edge-on density grid. Left: low-mixing regime. Right: high-mixing regime. White plus symbols represent the automatically detected edges; the position of the WR star is marked with a blue star; and the fit is shown as red dashed lines.

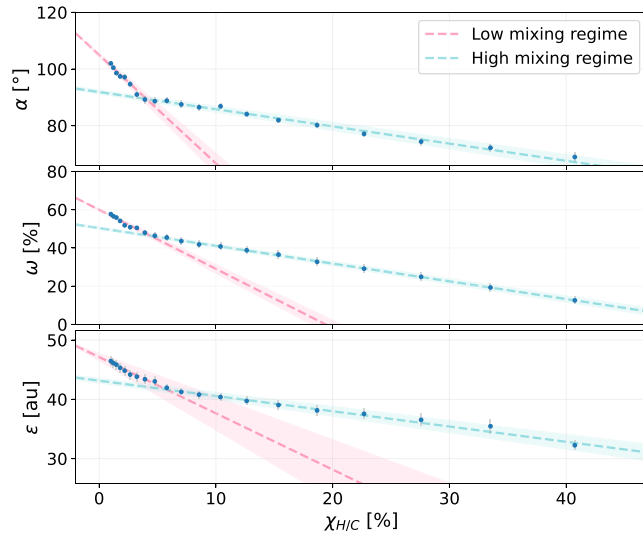


Figure 4. Evolution of the pinwheel parameters according to the hydrogen/carbon proportion ($\chi_{H/C}$). The presented parameters are the opening angle α , the filling factor ω , and the spiral width ϵ . The blue dots represent the measured values. The two regimes we identify are represented in pink (low mixing) and cyan (high mixing). Both linear fit parameters are shown in Table 3.

We identify two different regimes, hereafter referred to as the low- and high-mixing regimes. Both regimes can be remarkably well reproduced by a linear model, allowing us to estimate the opening angle for any mixing factor. We set two $\chi_{H/C}$ ranges ($1 < \chi_{H/C,1} < 4$ per cent, $5 < \chi_{H/C,2} < 40$ per cent) to fit the slope and the origin point (Table 3).

In the low-mixing regime (regime 1), the opening angle increases rapidly with the mixing factor. As the desired proportion of hydrogen is reduced, nucleation gets closer to the primary shock of the spiral. We can, therefore, push the hydrogen proportion to the limit of $\chi_H = 0.001$ per cent to be as close as possible to the fully carbonaceous region of the shock. Doing so yields $\alpha = 122^\circ \pm 1^\circ$, three times larger than the Eichler & Usov (1993) approximation. Hendrix et al. (2016) have already reported such a discrepancy in the comparable system of WR98a. Similarly, this high amplification of the opening angle appears to be caused by the effective cooling occurring in the shocked interface.

In the high-mixing regime (regime 2), the increase relative to $\chi_{H/C}$ is smoother and appears to be twice as big as the reported values of

Table 3. The fitted linear model used to represent the geometrical parameters. a and b refer to the slope and the origin point, respectively (i.e. $\alpha = a\chi_H + b$).

Parameter	Regime 1	Regime 2
Full-opening angle α	$a = -3.83 \pm 0.29$	$a = -0.61 \pm 0.04$
	$b = 104.9 \pm 0.6^\circ$	$b = 91.9 \pm 0.7^\circ$
Filling factor ω	$\chi_r^2 = 1.06$	$\chi_r^2 = 0.59$
	$a = -3.09 \pm 0.18$	$a = -0.93 \pm 0.03$
Arm width ϵ	$b = 60.0 \pm 0.4\%$	$b = 50.4 \pm 0.6\%$
	$\chi_r^2 = 2.64$	$\chi_r^2 = 0.12$
	$a = -0.95 \pm 0.22$	$a = -0.26 \pm 0.02$
	$b = 47.1 \pm 0.6$ au	$b = 43.1 \pm 0.4$ au
	$\chi_r^2 = 0.13$	$\chi_r^2 = 0.19$

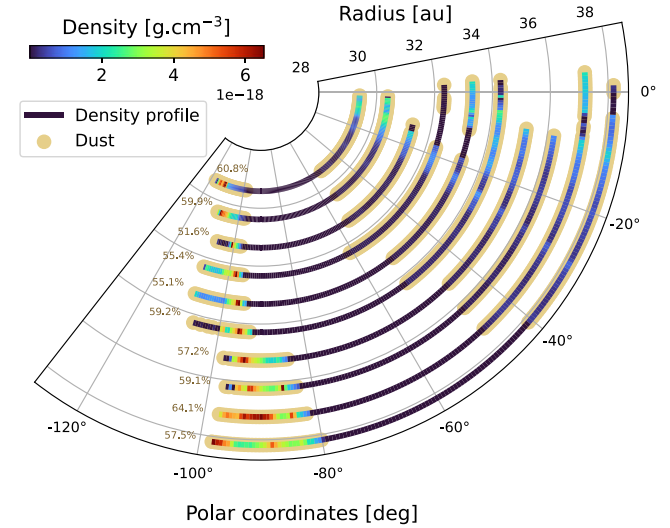


Figure 5. Density profiles in the middle-plane at different radii. The binary is located at the origin's axis ($R = 0$ au), not represented in this plot. The left/thinner side is the leading edge of the spiral (same orientation as in Fig. 6a). The detected dust is represented as beige dots. We show the measured fraction ω on the left of each profile.

$35^\circ/40^\circ$ obtained with high-angular-resolution observations (Tuthill et al. 2008; Soulain et al. 2018). Harries et al. (2004) reported that the opening angle should not exceed 80° , as constrained by masking interferometry data. These limiting values are still debated today owing to insufficient angular resolution and image fidelity, so we cannot entirely rule out the more extensive range of opening angles encompassed in this work.

4.1.2 Internal structure of the spiral

The mixed region considered to produce the dust forms an empty conical structure, represented by a filling factor ω . This new geometrical parameter denotes the relative wall thickness of the spiral and will play a central role in the brightness distribution at a larger scale. To investigate this parameter, we explore the mid-plane (YX -plane, Fig. 1) grid of the dust model to obtain a reasonable estimate of ω . The internal structure appears to be highly heckled and shows a large variety of thicknesses. Fig. 5 shows the internal density profile computed at different radii in the middle plane of the spiral. We determine the relative proportion of the dust included within both the leading and the trailing wall.

For each mixing regime, we compute the average and the standard deviation of the radially dependent ω . The considered uncertainties

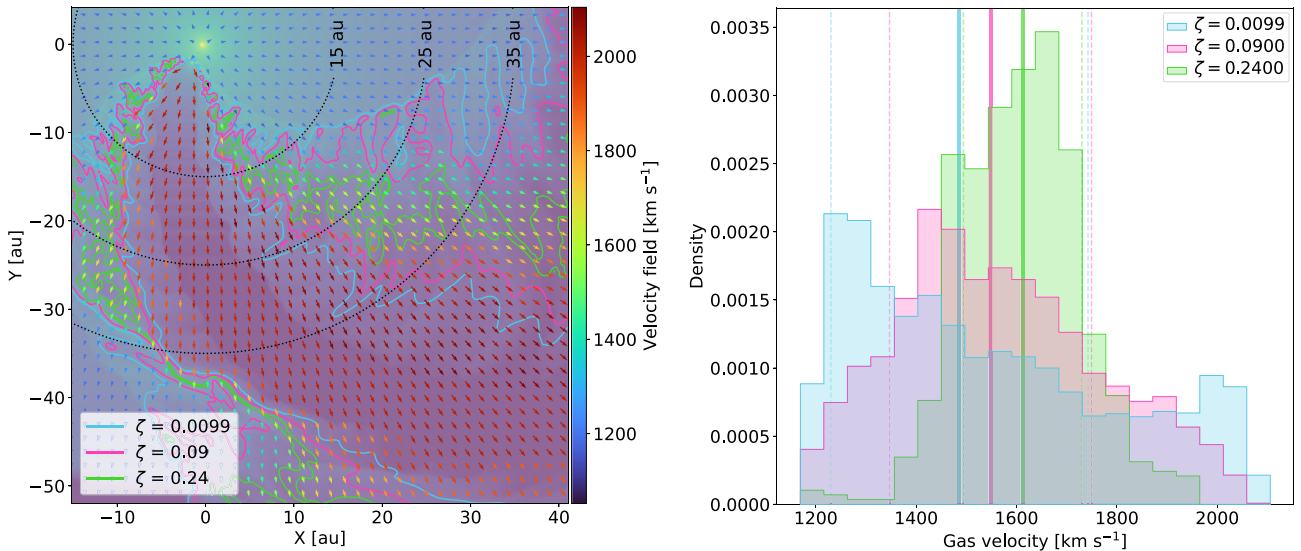


Figure 6. 2D map and associated distribution of the gas velocity along the orbital plane of the binary. (a) The underlying colour-scale layer shows the density map (low opacity). The quiver plot (overlaid arrows) represents the velocity field, in direction and amplitude, and is coloured according to the absolute wind speed (km s^{-1}). The coloured contours represent different mixing regime ζ (0.0099: 1–99 per cent; 0.09: 10–90 per cent; and 0.24: 40–60 per cent). Three possible dust nucleation radii are illustrated as black dashed lines. (b) The three colours represent the same mixing factor as in (a). The vertical lines are the average values, and the dashed lines are the standard deviation.

let us keep track of the radial distribution of ω . Anew, two regimes can be recognized and appear to be linearly dependent on χ_H . We note that the two regimes are localized in the same region as for the opening angle, suggesting a similar physical cause. Nonetheless, the transition around $\chi_H = 5$ per cent does not exhibit a significant slope difference (Fig. 4). The fitted linear coefficients a and b are presented in Table 3.

4.1.3 Face-on angle θ and arm width ϵ

In this section, we describe our investigation concerning the spiral arm width (ϵ in the following, Fig. 2). Despite the relatively limited simulated field size of our simulation, we were able to arrive at an estimate of this critical parameter using the face-on density image.

The first step consists of measuring the angular shift between the two sides of the spiral seen face-on. Both the leading and the trailing edge can be described by an Archimedean spiral, and the rotation between those two geometric spirals corresponds to the measurement of the face-on angle θ . We note that this measurement is supposed to be identical to the edge-on opening angle (α), but appears to be slightly different owing to projection effects. Therefore, we address this discrepancy by using an alternative method to measure the face-on opening angle θ , distinct from α reported above (Fig. 2). We measure θ using the polar density profiles at different radii (similar to Fig. 5 but on the summed face-on image). We used 10 profiles to determine the average value and its dispersion. Thus, θ is simply given by the angular distance between the two extremities of the profile above a threshold density value (i.e. the position of the Archimedean spiral associated with each side).

We then extrapolate the spiral shape at a large scale using an Archimedean spiral model to represent both edges of the spiral separated by the measured angle θ . To do so, we need to define the spiral step S of the Archimedean model. We explored different values to fit both the edges and the centre of the simulation. We determined that the best match is obtained with $S = 170$ au, which is fully consistent with the observations (170 ± 8 au; Soulain et al. 2018).

The arm width ϵ can then be measured as the linear distance between the two spiral models at a given azimuth (sufficiently far from the origin). The results are presented in Fig. 4. We fit the dependency of mixing using the same linear approximation method for both mixing regimes (Table 3).

4.2 Dust versus gas velocity

The dust velocity is typically attributed to the dominant terminal wind speed of the WR star (Tuthill et al. 1999, 2008). However, this strong hypothesis is still debated in the literature, and arguments exist for attributing the dust expansion to the weaker companion wind (Parkin & Pittard 2008; Harries et al. 2004). This assumption is particularly relevant to constraining the astrometric distance to the system. Indeed, the spiral step associated with the orbital period allows computation of the apparent angular velocity, which can be combined with the physical speed of the dust plume to yield the distance (Soulain et al. 2018). In this section, we use the velocity map rendered by the *RAMSES* code to investigate this hypothesis.

Fig. 6(a) shows the gas velocity in the binary orbital plane. The ‘quiver plot’ illustrates the amplitude and direction of the velocity field, whereas the colour indicates the value. In addition, we show the gas density map as the lower layer (with low opacity) as a location reference. For our purpose, we display as coloured contours the different layer of mixing ζ (cyan: 0.0099, 1 per cent–99 per cent; pink: 0.09, 10 per cent–90 per cent; and green: 0.24, 40 per cent–60 per cent).

We measure the velocity at the various expected locations of dust production (i.e. distance from the WR star) and for various mixing values. We report a similar velocity field across the various distances we tested (as shown by the dashed lines in Fig. 6a). The terminal wind speed is, as expected, already reached at the closest distance of 15 au. Therefore, the conclusion focused on the hydrogen dependency is uncorrelated with the nucleation radius (as reported in Section 4.3).

We find a high discrepancy between the two most extreme scenarios (1 and 40 per cent of the H-fraction, or the C-fraction, depending

Table 4. Velocities of the gas as a function of the mixing value ζ .

ζ	Median [km s ⁻¹]	Dispersion [km s ⁻¹]	Extremes [km s ⁻¹]
0.0099	1513	257	1069–2105
0.09	1548	204	1069–2080
0.24	1616	129	1168–1960

if the location is inside or outside the contact discontinuity). For the high-mixing regime, the gas velocity is perfectly balanced between the two stellar components, being about 1612 ± 117 km s⁻¹ (Table 4). The velocity is relatively constant within the highly mixed thin layer (green line in Fig. 6a). We measure a similar velocity field on both the leading and the trailing arm, with, however, a very strong gradient on the inner edge of the leading arm. The overall velocity field appears to be strongly correlated with the mixing ratio, exhibiting a similar gradient on both arms.

The low-mixing regime exhibits highly differential velocity values across the considered layer (inside the cyan line, Fig. 6a). The gas is dominated by the O-star component on the inner edge (1800–2000 km s⁻¹), whereas it is dominated by the WR wind on the outer edge (1000–1200 km s⁻¹). We report a median velocity of 1486 ± 256 km s⁻¹, where the indicated uncertainty denotes the dispersion of the distribution (Table 4). For comparison, we present the normalized distribution of the velocities between 15 and 40 au for three mixing values. The relatively flat distribution of the low-mixing scenario exhibits a large gas-speed dispersion across the spiral walls, whereas it peaks at about 1600 km s⁻¹ for the high-mixing one (Fig. 6b). The resulting dust expansion speed submitted to this differential velocity field between its edges could result in over-densities at larger scales.

4.3 Dust nucleation radius

In this section, we discuss the various constraints we have on the nucleation radius. Fig. 7 shows the relative proportion of hot cells compared with the nucleation radius and the gas-to-dust ratio for different dust composition hypotheses (in columns a to d) and grain sizes (in rows 1 to 3). For the specific combination of mixing ($\zeta = 0.0475$: 5–95 per cent) and grain sizes (*small* – see b1 in Fig. 7), the expected nucleation radius appears to be close to 30 au for the overall range of ξ_{dust} . We note the same behaviour for the other mixing values, with an expected nucleation radius of about 30–32.5 au (Fig. 7).

For a specific nucleation radius, an increase in mass reduces the relative proportion of hot dust while decreasing the maximum temperature. We note that the nucleation radius seems to be independent of the dust mass, in the range tested by our models. Regarding the maximum temperature, our models show quite comparable results for the H-fraction cases we explored. They differ from 2100 to 2800 K for the most extreme scenario, namely close to the star (15 au) and with the lowest mixing factor (1 per cent).

For the *large* grain-size scenario, Fig. 7 shows a nucleation radius closer to the star, between 20 and 22.5 au. A nucleation radius this close to the central source is very unlikely and can be excluded by observational constraints. The measured radius is expected to be even closer for the smallest gas-to-dust ratio we tested (0.1 per cent) and cannot be constrained by our model. The maximum temperatures are similar to in the previous case but can reach higher values, up to 3000 K, while affecting a larger fraction of mass (up to 5 per cent, against 2 per cent for the *small* grain-size scenario).

Finally, the *unique* grain-size scenario does not allow for any dust condensation in the parameters explored in Fig. 7. The four

H-fraction cases are always above the sublimation temperature of 2000 K, even for the tiniest mass fraction. Dust never condenses in such a case, but could condensate farther away (beyond the boundaries explored in this study). In addition, the maximum temperatures are much higher than in the two previous scenarios, standing between 2500 and 3700 K. The fraction of hot dust is also higher, up to 10 per cent. Interestingly, the fraction of hot dust increases with the H-fraction, in contrast to the two previous scenarios.

5 DISCUSSION

Despite only simulating a finite circumstellar volume around the WR 104 binary, dedicated to the innermost regions, we have recovered several insights into the system’s properties.

5.1 Proxy of dust nucleation process

Based on purely geometrical arguments, our RAMSES simulation suggests the presence of two distinct nucleation regimes, depending on the gas’s hydrogen fraction. All three geometrical parameters explored in our study (namely the opening angle α , the filling factor ω , and the spiral arm width ϵ) appear to be linearly correlated with the mixing factor (ζ). The first regime, which we called the ‘low-mixing regime’, corresponds to a relatively fast decrease of the parameter with respect to the $\chi_{\text{H/C}}$. For instance, the opening angle changes from 105° to 90° on the first 5 per cent of hydrogen variation, while falling to 70° at the maximum considered H-fraction. Such a discrepancy, between the low and high regimes, appears less important for the two other quantities, which are less affected by the geometry of the external spiral walls. For the most extreme case ($\chi_{\text{H/C}} = 1$ per cent), the dust locus reaches the interface between the gaseous spiral cone and the WR free-wind-dominated region. Such regions can be subject to various hydrodynamic instabilities. They are responsible for the wavy aspect of the shocked region in the 3D grid in Fig. 1. The velocity difference between the winds leads to the development of the Kelvin–Helmholtz instability. As the velocity gradient at the interface is small, the growth of the instability remains small, and the instability is linear (Lamberts et al. 2011). Such unsteady interface physics could explain the reported difference between the two regimes.

The two regimes we identified represent a good proxy for the nucleation processes, which can be compared with observational constraints. All previous studies that focused on pinwheel nebulae (Monnier et al. 1999; Tuthill et al. 2008; Soulain et al. 2018; Lau et al. 2020b) reported various estimates of morphological parameters (e.g. the opening angle from 40° to 120°). With our study, we propose to correlate such geometrical measurements with underlying physical properties represented by the mixing factor ζ . In particular, the opening angle seems to exhibit a large variation depending on the H/C-fraction and could therefore represent a sensitive diagnostic of the nucleation processes.

Additionally, we reported a new estimate of the value of the filling factor. This important parameter is widely considered in the literature but is without a clear definition. Tuthill et al. (2008) and Soulain et al. (2018) reported an empty spiral structure bounded by an infinitely thin surface sheet – an approximation that entirely sidesteps any filling proportion arguments. In our study, we reported values ranging from 20 per cent to 60 per cent, which may significantly affect the intensity profile of the spiral arm.

We addressed the question of the spiral arm width by analysing the projected opening angle at a larger scale. The arm width is usually derived from the opening angle of the wind collision zone

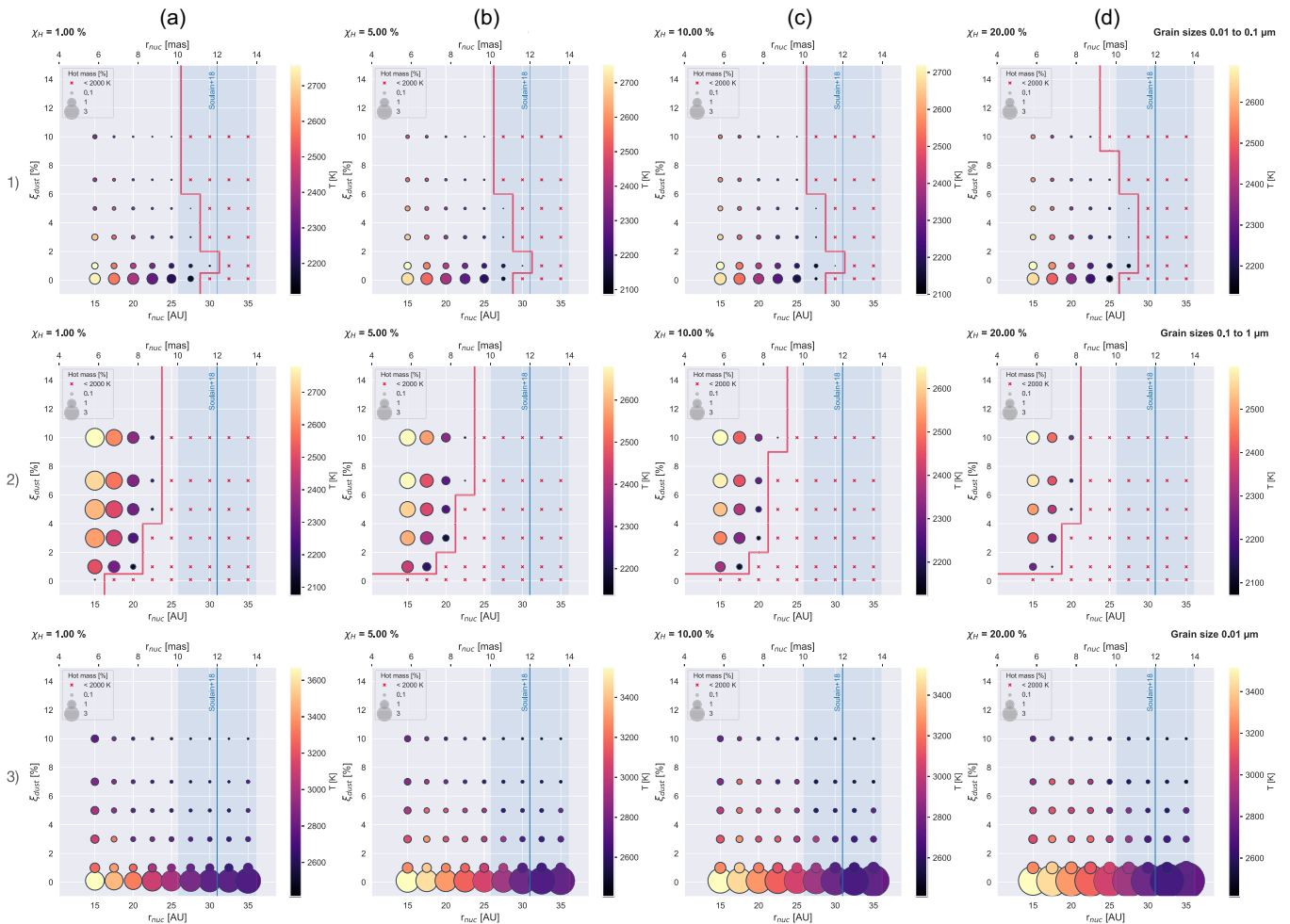


Figure 7. Maximum temperature (colour gradient) and hot cell fraction (scatter size) compared with the nucleation radius and the gas-to-dust ratio. Each dot corresponds to one of the 648 radiative transfer models computed in this work. The red crosses represent the case where the dust temperature is below the sublimation limit of 2000 K. From left to right: mixing values from 1 to 20 per cent. Top: *small* grain-size hypothesis. Middle: *large* grain-size hypothesis. Bottom: *unique* grain-size hypothesis. The red line corresponds to the predicted nucleation radius determined in this work. The observational estimate is shown in blue for comparison (Soulain et al. 2018).

in a purely geometrical approach. In this study, we reported a more realistic determination by considering the 3D aspect of the deformed cone. The opening angle seemed slightly different between the orbital plane view and the orthogonal polar plane. The reported width corresponds to the orbital plane, where the spiral is seen face-on. Fig. 4 reveals the imperfect correlation between the opening angle of the shock (not deformed by the orbital motion) and the large-scale spiral arm width. Therefore, observers should assess the typical correlation between these two fundamental aspects and carefully consider the degree of projection in deriving their model. The linear correlation found in this work can accordingly be used as a calibration hypothesis to retrieve the accurate opening angle from the spiral width determination, and vice versa.

5.2 Dust nature and nucleation temperature

The radiative transfer modelling allows us to obtain an independent measurement of the nucleation radius. This crucial parameter appears to be not related to the dust-to-gas ratio (i.e. the density); the latter only affects the proportion of ‘hot’ dust in the simulation. Considering the observational estimates of the nucleation radius

(10–14 mas; Tuthill et al. 2008; Soulain et al. 2018), we are able to draw conclusions about the nature of the dust grains, which are compatible with a small-grain-size distribution (0.01–0.1 μm). When considering a unique grain size (0.01 μm), the absence of nucleation lets us rule out the hypothesis of no evolution (Zubko 1998). We note that our favoured small-grain-size distribution appears to be contra the work of Lau et al. (2020a), which focused on the analysis of the SED on a sample of WC stars.

The nature of the dust around WR stars appears to be different from that of the interstellar dust (Kim, Martin & Hendry 1994), young stellar objects (Kraus et al. 2010), or the AGB dust (Ferrarotti & Gail 2006; Ventura et al. 2020). Regarding the dust species formed in oxygen-rich environments (e.g. stars on the AGB), the most stable compounds are silicates, alumina dust (Al_2O_3), and solid iron. In the case of WR stars, C-rich species are favoured by formation pathways through the PAH reaction and should have a limited size distribution owing to their rapid growth and subsequent rapid injection (1200–1600 km s^{-1}) into the interstellar medium.

The carbonaceous dust could have a larger than predicted impact on the overall dust amount of galaxies (Matsuura et al. 2009; Boyer et al. 2012; Lau et al. 2020a), redistributing the energetic stellar

budget in a different manner (by way of absorption efficiency and diffusion). In the context of galactic chemistry, the presence of moderate-size grains (0.01–0.1 μm) could favour the transport of alumina isotopes in solar-type nebulae (Dwarkadas et al. 2017). Depending on the total contribution of the dust of WR origin in the interstellar medium, bigger and more resistant carbonaceous grains should have a non-negligible impact on the destruction time-scale of interstellar dust. More specifically, larger carbon grains could survive to the supernova and post-supernova shock (Nozawa, Kozasa & Habe 2006; Lazzati & Heger 2016) following the WR stage of massive stars and could therefore contribute significantly to the dust enrichment of galaxies. This is especially true of the early Universe, where the total amount of massive stars was significantly higher than it is today (Morgan & Edmunds 2003).

5.3 Differential velocity versus clumpy spiral plume

We saw that, depending on the dust nucleation pathways, newly formed dusty grains can be ejected at different speeds (Fig. 6b). For the most extreme scenario, the velocity could exhibit a strong gradient ranging from 1200 to 2000 km s^{-1} . If some dusty structures are faster at their birth origins, some overlap could therefore appear after some orbital revolutions. Such over-densities are hardly distinguishable from the projection effect showing brighter spiral edges (Hendrix et al. 2016) and should be explored at larger scales. Recent simulation studies, such as those by Eatson, Pittard & Van Loo (2022), report a very clumpy dusty structure that could be addressed by such differential velocity origins.

5.4 Leakage of dust and instabilities

The external walls of the spiral wind interface appear to be dominated by the Kelvin–Helmholtz instability. The effect of the instability can be seen in Fig. 1, as large plumes or ‘fingers’ escaping the spiral cone. These fingers were previously reported by Madura et al. (2015), using a Smoothed particle hydrodynamics simulation of the Eta Carinae system, and by Lamberts et al. (2012) using the `RAMSES` code on a variety of wind parameters. In theory, such instabilities should be able to carry dust particles out of the confined gaseous spiral and enrich the nebulae all around the binary system. We inspected the previous stage of our simulation to retrieve the previous positions of these plumes. Our simulation spans just enough time to retrieve the spiral deformation resulting from the orbit; however, past stages are not sufficiently advanced to be used at a confident level. Nevertheless, these structures are present in the previous output but appear smaller and closer to the star. Therefore, they could fill up the entire domain of the simulation after a few orbits. This phenomenon could amplify the dust nucleation process occurring within the pure WR wind, as recently reported in the hydrodynamical simulation of various colliding-wind binaries (Eatson et al. 2022). Such global structure has been reported around various colliding binaries using long-baseline interferometry techniques (Millour et al. 2009; Soulain et al. 2016). Such studies indicate the presence of an extended dust ‘halo’ responsible for very low-visibility measurements recovered by interferometry. We are actively investigating whether such a halo can be attributed to a fully resolved circumstellar shell; however, such results lie beyond the scope of this paper, and we defer discussion to a later publication.

6 CONCLUSIONS

Inspired by observational findings for the WR 104 system, we have used hydrodynamical simulations and radiative-transfer post-

processing to study the properties of the dust nucleation process occurring around massive evolved binary stars. We investigated the 3D structure of the colliding-wind binary in the innermost region where dust is expected to form. Below, we summarize our most important results.

(i) We report a direct correlation between the observable parameters governing the form of the observed spiral plume (opening angle, spiral width, and filling factor) and the chemical composition of the gas, represented by the hydrogen fraction supplied by the O-type star companion.

(ii) The velocity field shows a differential structure that could challenge the standard assumption about the terminal wind speed of such systems. Depending on the dust nucleation locus (i.e. the H-fraction), the projected velocity of the dust can present a strong gradient (1200–2000 km s^{-1}) or a more balanced speed (1600 km s^{-1}). Such discrepancies should be carefully considered when comparing the spectroscopic measurement of the stellar wind speed and the projected dust speed.

(iii) The nucleation radius stands at around 25–30 au if we consider the small-grain-size distribution (0.01–0.1 μm), in close agreement with the observational constraints. The chemical nature of the dust around WR stars diverges from that of other commonly encountered dust-producing systems in the galaxy, a finding that could have a non-negligible impact on galactic dust composition.

(iv) High levels of instability at the shock interface create finger structures that, in turn, could facilitate the escape of material through the collimated gaseous wall. This may carry dust outside the spiral and could precipitate the presence of a dusty ‘halo’ around colliding-wind binary systems, for which observational support already exists from interferometry.

We have demonstrated in this paper how hydrodynamical simulation is a critical tool for understanding the physics of these complex astrophysical systems. The realistic 3D view obtained with the `RAMSES` code can then be post-processed by a radiative-transfer code to extract the valuable quantities. Colliding-wind binary systems represent a challenging science application, requiring diverse time-scales and spatial scales and the inclusion of a multitude of physical phenomena (e.g. radiative cooling, instabilities, dust opacity). The WR 104 system appears even more complex than anticipated, with the reported differential velocities, internal structure, and grain-size distribution. WR stars could be a major contributor to dust enrichment within galaxies, especially through seeding the interstellar medium with small grains ($< 0.1 \mu\text{m}$). Finally, with this work, we offer a way to trace the physical processes of dust nucleation by using only the geometrical parameters quantifiable using high-angular-resolution techniques (e.g. interferometry, adaptive optics imaging). As we hope this paper has illustrated, there is a very strong motivation to consider these fascinating WR systems carefully for their deep reach into the physics of dust formation and the wider implications for and beyond our own Galaxy.

ACKNOWLEDGEMENTS

We acknowledge support from the Australian Research Council (DP 180103408) that funded this work. This project was concluded thanks to funding from the European Research Council (ERC) under the European Union’s Horizon 2020 research and innovation programme (grant agreement no. 742095; SPIDI: Star–Planets–Inner Disk Interactions, <http://www.spidi-eu.org>). AL acknowledges funding from the Agence Nationale de la Recherche (ANR) through the COSMERGE grant ANR-20-CE31-001 as well as the ‘Programme National des Hautes Energies’ (PNHE) of CNRS/INSU co-funded by

CEA and CNES. FM acknowledges funding from the ANR through the MASSIF project ANR-21-CE31-0018-01. This research made use of NASA’s Astrophysics Data System SCIPY (Virtanen et al. 2020), NUMPY (Harris et al. 2020), MATPLOTLIB (Hunter 2007), and ASTROPY, a community-developed core PYTHON package for astronomy (Astropy Collaboration et al. 2018).

DATA AVAILABILITY

The hydrodynamical models (RAMSES format) computed for this article will be shared on reasonable request to the corresponding author. The PYTHON software used to interface RAMSES with the radiative transfer code RADMC3D is available at <https://github.com/Drsoulain/ASRADMC>. The post-processed RADMC3D grids (fits files) will be shared on request to the corresponding author.

REFERENCES

- Allen D. A., Swings J. P., Harvey P. M., 1972, *A&A*, 20, 333
 Astropy Collaboration et al., 2018, *AJ*, 156, 123
 Baldwin J. E., Haniff C. A., Mackay C. D., Warner P. J., 1986, *Nature*, 320, 595
 Bjorkman J. E., Wood K., 2001, *ApJ*, 554, 615
 Bladh S., Eriksson K., Marigo P., Liljegren S., Aringer B., 2019, *A&A*, 623, A119
 Boyer M. L. et al., 2012, *ApJ*, 748, 40
 Castellanos-Ramírez A., Rodríguez-González A., Meliani Z., Rivera-Ortiz P. R., Raga A. C., Cantó J., 2021, *MNRAS*, 507, 4044
 Castelli F., Kurucz R. L., 2004, in Piskunov N., Weiss W. W., Weiss D. F., eds, Proc. IAU Symp. No 210, Modelling of Stellar Atmospheres, Modelling of Stellar Atmospheres, Poster Contributions. Cambridge Univ. Press, Cambridge, p. A20
 Cherchneff I., Le Teuff Y. H., Williams P. M., Tielens A. G. G. M., 2000, *A&A*, 357, 572
 Chiar J. E., Tielens A. G. G. M., 2001, *ApJ*, 550, L207
 Crowther P. A., 1997, *MNRAS*, 290, L59
 Dhanoa H., Rawlings J. M. C., 2014, *MNRAS*, 440, 1786
 Dsilva K., Shenar T., Sana H., Marchant P., 2020, *A&A*, 641, A26
 Dullemond C. P., Juhasz A., Pohl A., Sereshti F., Shetty R., Peters T., Commercon B., Flock M., 2012, Astrophysics Source Code Library, record ascl:1202.015
 Dwarkadas V. V., Dauphas N., Meyer B., Boyajian P., Bojazi M., 2017, *ApJ*, 851, 147
 Eatson J. W., Pittard J. M., Van Loo S., 2022, *MNRAS*, 516, 6132
 Eichler D., Usov V., 1993, *ApJ*, 402, 271
 Ferrarotti A. S., Gail H. P., 2006, *A&A*, 447, 553
 Fierro C. R., Borissova J., Zsargó J., Díaz-Azuara A., Kurtev R., Georgiev L., Ramírez Alegría S., Peñaloza F., 2015, *PASP*, 127, 428
 Gaia Collaboration et al., 2018, *A&A*, 616, A1
 Gobrecht D., Cristallo S., Piersanti L., Bromley S. T., 2017, *ApJ*, 840, 117
 Groh J. H., Meynet G., Ekström S., Georgy C., 2014, *A&A*, 564, A30
 Han Y. et al., 2020, *MNRAS*, 498, 5604
 Harries T. J., Monnier J. D., Symington N. H., Kurosawa R., 2004, *MNRAS*, 350, 565
 Harris C. R. et al., 2020, *Nature*, 585, 357
 Heays A. N., Bosman A. D., van Dishoeck E. F., 2017, *A&A*, 602, A105
 Hendrix T., Keppens R., van Marle A. J., Camps P., Baes M., Meliani Z., 2016, *MNRAS*, 460, 3975
 Howarth I. D., Schmutz W., 1992, *A&A*, 261, 503
 Hunter J. D., 2007, *Comput. Sci. Eng.*, 9, 90
 Kim S.-H., Martin P. G., Hendry P. D., 1994, *ApJ*, 422, 164
 Kobayashi H., Kimura H., Watanabe S.-i., Yamamoto T., Müller S., 2011, *Earth, Planets, Space*, 63, 1067
 Kraus S. et al., 2010, *Nature*, 466, 339
 Lamberts A., Fromang S., Dubus G., 2011, *MNRAS*, 418, 2618

- Lamberts A., Dubus G., Lesur G., Fromang S., 2012, *A&A*, 546, A60
 Lamberts A. et al., 2017, *MNRAS*, 468, 2655
 Lau R. M., Eldridge J. J., Hankins M. J., Lamberts A., Sakon I., Williams P. M., 2020a, *ApJ*, 898, 74
 Lau R. M. et al., 2020b, *ApJ*, 900, 190
 Lau R. M. et al., 2021, *ApJ*, 909, 113
 Lazzati D., Heger A., 2016, *ApJ*, 817, 134
 Myasnikov A. V., Zhekov S. A., 1993, *MNRAS*, 260, 221
 Madura T. I., Clementel N., Gull T. R., Kruij C. J. H., Paardekooper J. P., 2015, *MNRAS*, 449, 3780
 Maercker M. et al., 2012, *Nature*, 490, 232
 Marchenko S. V., Moffat A. F. J., Vacca W. D., Côté S., Doyon R., 2002, *ApJ*, 565, L59
 Matsuura M. et al., 2009, *MNRAS*, 396, 918
 Millour F. et al., 2009, *A&A*, 506, L49
 Min M., Hovenier J. W., de Koter A., 2005, *A&A*, 432, 909
 Monnier J. D., Tuthill P. G., Danchi W. C., 1999, *ApJ*, 525, L97
 Monnier J. D., Greenhill L. J., Tuthill P. G., Danchi W. C., 2002, *ApJ*, 566, 399
 Morgan H. L., Edmunds M. G., 2003, *MNRAS*, 343, 427
 Nozawa T., Kozasa T., Habe A., 2006, *ApJ*, 648, 435
 Parkin E. R., Pittard J. M., 2008, *MNRAS*, 388, 1047
 Parkin E. R., Pittard J. M., 2010, *MNRAS*, 406, 2373
 Pinte C., Harries T. J., Min M., Watson A. M., Dullemond C. P., Woitke P., Ménard F., Durán-Rojas M. C., 2009, *A&A*, 498, 967
 Pittard J. M., 2009, *MNRAS*, 396, 1743
 Pittard J. M., Dougherty S. M., Coker R. F., Corcoran M. F., 2005, in Sjouwerman L. O., Dyer K. K., eds, X-Ray and Radio Connections. NRAO, Santa Fe, NM, p. 2.01
 Rate G., Crowther P. A., 2020, *MNRAS*, 493, 1512
 Rosslove C. K., Crowther P. A., 2015, *MNRAS*, 447, 2322
 Rowlands K., Gomez H. L., Dunne L., Aragón-Salamanca A., Dye S., Maddox S., da Cunha E., van der Werf P., 2014, *MNRAS*, 441, 1040
 Sana H. et al., 2013, *A&A*, 550, A107
 Sander A., Hamann W.-R., Todt H., 2012, *A&A*, 540, A144
 Sander A. A. C., Hamann W. R., Todt H., Hainich R., Shenar T., Ramachandran V., Oskinova L. M., 2019, *A&A*, 621, A92
 Soulain A., Millour F., Lopez B., Lagadec E., Matter A., Hofmann K. H., 2016, in Malbet F., Creech-Eakman M. J., Tuthill P. G., eds, Soc. Photo-Opt. Instrum. Eng. (SPIE) Conf. Ser. Vol. 9907, Optical and Infrared Interferometry and Imaging V. SPIE, Bellingham, p. 99073R
 Soulain A. et al., 2018, *A&A*, 618, A108
 Srinivasan S., Boyer M. L., Kemper F., Meixner M., Sargent B. A., Riebel D., 2016, *MNRAS*, 457, 2814
 Stevens I. R., Blondin J. M., Pollock A. M. T., 1992, *ApJ*, 386, 265
 Sutherland R. S., Dopita M. A., 1993, *ApJS*, 88, 253
 Tatischeff V., Duprat J., de Sérville N., 2010, *ApJ*, 714, L26
 Teyssier R., 2002, *A&A*, 385, 337
 Tuthill P. G., Monnier J. D., Danchi W. C., 1999, *Nature*, 398, 487
 Tuthill P. G., Monnier J. D., Danchi W. C., Wishnow E. H., Haniff C. A., 2000, *PASP*, 112, 555
 Tuthill P. G., Monnier J. D., Lawrance N., Danchi W. C., Owocki S. P., Gayley K. G., 2008, *ApJ*, 675, 698
 Usov V. V., 1991, *MNRAS*, 252, 49
 van Marle A. J., Keppens R., 2011, *Comput. Fluids*, 42, 44
 Ventura P., Dell’Agli F., Lugaro M., Romano D., Tailo M., Yagüe A., 2020, *A&A*, 641, A103
 Virtanen P. et al., 2020, *Nature Methods*, 17, 261
 Wallace D. J., Moffat A. F. J., Shara M. M., 2002, in Moffat A. F. J., St-Louis N., eds, ASP Conf. Ser. Vol. 260, Interacting Winds from Massive Stars. Astron. Soc. Pac., San Francisco, p. 407
 Williams P. M., van der Hucht K. A., The P. S., 1987, *A&A*, 182, 91
 Williams P. M. et al., 2009, *MNRAS*, 395, 1749
 Zubko V. G., 1998, *MNRAS*, 295, 109

This paper has been typeset from a $\text{\TeX}/\text{\LaTeX}$ file prepared by the author.